processes

MDPI

Article

The Effect of Sodium Tetrafluoroborate on the Properties of Conversion Coatings Formed on the AZ91D Magnesium Alloy by Plasma Electrolytic Oxidation

Łukasz Florczak [1,*], Ginter Nawrat [2], Kazimierz Darowicki [3], Jacek Ryl [4], Jan Sieniawski [5], Małgorzata Wierzbińska [5], Krzysztof Raga [6] and Andrzej Sobkowiak [1,*]

[1] Department of Physical Chemistry, Faculty of Chemistry, Rzeszow University of Technology, 35-959 Rzeszow, Poland
[2] Faculty of Chemistry, Silesian University of Technology, 44-100 Gliwice, Poland
[3] Faculty of Chemistry, Gdansk University of Technology, 80-233 Gdansk, Poland
[4] Faculty of Applied Physics and Mathematics, Gdansk University of Technology, 80-233 Gdansk, Poland
[5] Faculty of Mechanical Engineering and Aeronautics, Rzeszow University of Technology, 35-959 Rzeszow, Poland
[6] Pratt & Whitney Rzeszow, 35-078 Rzeszow, Poland
* Correspondence: l.florczak@prz.edu.pl (Ł.F.); asobkow@prz.edu.pl (A.S.)

Abstract: Magnesium and its alloys are widely used in many areas because of their light weight, excellent dimensional stability, and high strength-to-weight ratio. However, the material exhibits poor wear and corrosion resistance, which limits its use. Plasma electrolytic oxidation (PEO) is an effective surface modification method for producing ceramic oxide layers on Mg and their alloys. The influence of the additions of sodium tetrafluoroborate ($NaBF_4$) and sodium fluoride (NaF) into alkaline-silicate electrolyte on the properties of the conversion layers formed in the magnesium AZ91D alloy has been investigated. Surface morphology and chemical composition were determined by scanning electron microscopy (SEM) and X-ray photoelectron spectroscopy (XPS). The anticorrosive properties of the layers were evaluated by electrochemical impedance spectroscopy (EIS) and potentiodynamic polarization (PDP) methods in simulated body fluid (SBF). The presence of $NaBF_4$ or NaF in the electrolyte increases the corrosion resistance of the protective layer. However, the best anticorrosive properties show the layers obtained in the presence of $NaBF_4$. This is probably caused by the incorporation of boron and fluorine in the form of Mg $(BF_4)_2$ mainly in the barrier layer.

Keywords: magnesium alloy; plasma electrolytic oxidation; tetrafluoroborate; corrosion resistance

Citation: Florczak, Ł.; Nawrat, G.; Darowicki, K.; Ryl, J.; Sieniawski, J.; Wierzbińska, M.; Raga, K.; Sobkowiak, A. The Effect of Sodium Tetrafluoroborate on the Properties of Conversion Coatings Formed on the AZ91D Magnesium Alloy by Plasma Electrolytic Oxidation. *Processes* **2022**, *10*, 2089. https://doi.org/10.3390/pr10102089

Academic Editor: Prashant K. Sarswat

Received: 15 September 2022
Accepted: 12 October 2022
Published: 15 October 2022

1. Introduction

Magnesium and its alloys are characterized by low density, high strength-to-weight ratio, dimensional stability, high impact resistance, and good thermal and electrical conductivity. These properties determine the applications of materials in the areas in which weight reduction or high technical requirements are needed, including automotive and aerospace industries and biomedical applications. However, magnesium and its alloys have important disadvantages, which limit their use: poor wear resistance, low hardness, and poor anticorrosion properties [1–3].

To increase hardness and especially corrosion resistance, different methods are used for the formation of protective coatings on the surface of the materials [4,5]. These are, among others: chemical conversion [6], electrophoretic deposition [7], hydrothermal treatment [8], chemical vapor deposition [9], electrodeposition [10], sol-gel process [11], and organic compounds deposition [12]. Among many possible and accessible coating methods to improve the corrosion resistance of magnesium alloys, plasma electrolytic oxidation (PEO), also known as the microarc oxidation (MAO) procedure, is a common technique due to its environmental friendliness and high performance [13–18].

During the process, electrical discharges in aqueous solutions cause the formation of a protective layer on the surface of the material, which consists mainly of its oxides, but modifying elements present in the electrolyte are frequently incorporated into the protective layer. Therefore, in addition to parameters such as current characteristics, temperature, and time of treatment, the type of electrolyte is a key aspect that influences the quality of the coating produced in PEO processes [19].

The solution of sodium metasilicate (Na_2SiO_3) with sodium hydroxide is commonly used as an electrolyte for PEO processes [20–23]. The addition of fluoride ions to the electrolyte solution affects the composition, structure, and morphology of the conversion coatings formed and consequently the mechanical, tribological, and anticorrosion properties and their performance [24–27]. In recent years, novel additives for the basic electrolyte have been applied that contain, in addition to fluorine, other elements in the form of single salts such as K_2ZrF_6 [28], K_2TiF_6 [29], Na_2SiF_6 [30], Na_3AlF_6 [31]. There are also studies that show a positive effect of sodium tetraborate [32–35] and sodium pentaborate [36] on the properties of coatings. The results of these studies show that the presence of fluorine or boron compounds in the electrolyte improves the mechanical and anticorrosive properties of the coatings obtained. Therefore, we have expected that a synergetic effect can exist when both elements are present in the electrolyte. Sodium tetrafluoroborate has been chosen since we have recently found that the addition of $NaSbF_6$ to the Na_2SiO_3-based electrolyte causes the incorporation of antimony into a protective layer formed on the magnesium alloy AZ91D by the PEO process and increases the corrosion resistance of the layer [37].

Here, we report the results on the influence of $NaBF_4$ and NaF in amounts having the same fluorine content in the alkaline-silicate electrolyte on the physicochemical properties and corrosion resistance of the conversion layers formed under the same conditions.

2. Materials and Methods

2.1. Preparation of Specimens

The AZ91D magnesium alloy was cut into rectangular specimens of dimensions 50 × 50 × 10 mm and used as a substrate material. The chemical composition of the alloy identified by the analysis using a Thermo Scientific (Waltham, MA, USA) ARL ADVANT XP Sequential X-Ray Fluorescence Spectrometer (XRF) is listed in Table 1. The surfaces of all samples were ground with 600 to 1200-grit SiC paper to ensure uniform surface roughness. The samples were then washed in deionized water, ultrasonically degreased with acetone, and dried. Subsequently, they were electrochemically activated as anodes in saturated NaF solution for 5 min at a voltage equal to 60 V (DC). Immediately after this procedure, the sample was rinsed with deionized water and submitted to the PEO process.

Table 1. Chemical composition of the AZ91D alloy.

The Content of Elements, wt.%								
Al	**Zn**	**Mn**	**Si**	**Ca**	**Fe**	**Ni**	**Cu**	**Mg**
8.77	0.74	0.18	<0.01	<0.01	<0.001	<0.001	<0.001	balance

2.2. Plasma Electrolytic Oxidation (PEO) Process

The base electrolyte solution was composed of 15 g/L of $Na_2SiO_3 \cdot 5H_2O$ and 4.2 g/L of NaOH in deionized water. Investigated $NaBF_4$ or NaF was added to the base electrolyte in quantities to ensure an equimolar amount of fluorine. Table 2 lists the composition of the three electrolytes, their conductivity, and the corresponding identification codes of the samples treated in these electrolytes. All solutions were prepared using commercially available analytical grade reagents and deionized water (conductivity below 0.1 μS/cm at 25 °C).

Table 2. The identification codes for the PEO coatings with their respective electrolyte composition and conductivity.

Sample Code	Composition of Electrolyte, g/L	Molar Concentration of Fluorine, mM/L	Conductivity of Electrolyte, mS/cm
Base	$Na_2SiO_3 \cdot 5H_2O$: 15 NaOH: 4.2	-	32.1
BF4	$Na_2SiO_3 \cdot 5H_2O$: 15 NaOH: 4.2 $NaBF_4$: 2	72.9	33.1
F	$Na_2SiO_3 \cdot 5H_2O$: 15 NaOH: 4.2 NaF: 3.06	72.9	35.3

2.3. Characterization of the Coatings

Surface and cross-sectional morphologies of the PEO coatings were characterized using a HITACHI S-3400N (Tokyo, Japan) scanning electron microscope (SEM). Image analysis was performed using ImageJ 1.46r software. Image filtering was applied to remove noise followed by image segmentation by thresholding, which produced binary images. Subsequently, the average total outer porosity, the average outer pore size, and the outer pore size distribution were calculated. An eddy current coating thickness measurement gauge, Fischer Dualscope (Sindelfingen, Germany) MP20 with FTA 3.3H sonde, was used to measure the thickness of the coatings. The average layer thickness and standard derivation of each sample were calculated from 20 measurements.

The elemental analysis was performed using an energy-dispersive X-ray spectrometer (EDS) attached to an SEM. The chemical states of the PEO coatings were determined using Escalab 250Xi Thermofisher Scientifican X-ray photoelectron spectroscopy (XPS) with a Kα anode (λ = 1486.6 eV). In XPS analysis, sputtering was conducted with an argon ion gun to obtain a depth profile of the coating. All energy values were corrected according to the adventitious C 1s set at 284.6 eV.

Potentiodynamic polarization (PDP) and electrochemical impedance spectroscopy (EIS) tests were applied to evaluate the corrosion performance of the coatings in a simulated body fluid (SBF). The composition of the SBF is given in Table 3 [38]. The electrolyte temperature was maintained at 36.5 $\pm$ 0.5 °C. Electrochemical corrosion tests were carried out using a PARSTAT 2273 (Princeton Applied Research) in a conventional three-electrode cell (200 mL) with the sample as the working electrode (exposed area of 0.785 cm^2), a platinum mesh serving as an auxiliary electrode, and a silver chloride electrode immersed directly in a corrosive solution as the reference electrode (+34 mV vs. SCE). Before electrochemical measurements, the samples were immersed in the SBF solution for 3 h to allow the open circuit potential (OCP) to become stable. Polarization curves were collected at a scanning rate of 1 mV/s from -0.25 V to +0.25 V versus OCP. Electrochemical parameters, including corrosion potential (E_{CORR}), corrosion current density (j_{CORR}), and Tafel slopes, were determined using the Tafel extrapolation method. Polarization resistance (R_P) was calculated according to the Stern–Geary equation (Equation (1)) [39]:

$$R_P = \frac{\beta_A \cdot \beta_c}{2.3 \cdot j_{CORR}(\beta_A + \beta_C)} \quad (1)$$

Table 3. Composition of the simulated body fluid (SBF) [38].

Concentration of Compounds, g/L								
NaCl	$NaHCO_3$	KCl	$K_2HPO_4 \cdot 3H_2O$	$MgCl_2 \cdot 6H_2O$	$CaCl_2$	Na_2SO_4	$(CH_2OH)_3CNH_2$	HCl (1.0 M)
8.035	0.355	0.225	0.231	0.311	0.292	0.072	6.118	Adjusted pH to 7.4

Because the vulnerability of a coating to an aggressive environment is directly connected with the number of pores, the porosity of the coated surfaces was also determined using the potentiodynamic polarization method. In this case, the porosity (F) is defined by Equation (2) [40–42]:

$$F = \frac{R_{P,S}}{R_{P,C}} \cdot 10^{-\left(\frac{|\Delta E_{CORR}|}{\beta_A}\right)} \quad (2)$$

where $R_{P,S}$ and $R_{P,C}$ are the polarization resistance of the uncoated and coated samples, respectively, ΔE_{CORR} is the difference in the corrosion potential between the coated and uncoated samples, and β_A is the Tafel anodic slope of the uncoated sample.

The electrochemical impedance curves were obtained by applying a sinusoidal potential of 10 mV (rms) in amplitude around OCP in steady state, in the frequency range from 100 kHz to 100 mHz. The experimental results were interpreted assuming an equivalent circuit using a suitable fitting procedure implemented in the ZSimpWin 3.21 software (Ann Arbor, MI, USA). These measurements were repeated a total of at least three times for each sample to determine the repeatability of the results. To examine the dependability, causality, and stability of the real EIS data obtained from the experimental process, the Kramers–Kronig (K–K) transformations were applied with the KK Test 1.01 software (B. A. Boukamp). The Kramers–Kronig relations are defined as follows [43]:

$$Z'(\omega) = Z'(\infty) + \frac{2}{\pi}\int_0^\infty \frac{xZ''(x) - \omega Z''(\omega)}{x^2 - \omega^2} dx \quad (3)$$

$$Z''(\omega) = -\left(\frac{2\omega}{\pi}\right)\int_0^\infty \frac{Z'(x) - Z'(\omega)}{x^2 - \omega^2} dx \quad (4)$$

where: Z'—the real parts of the impedance, Z''—the imaginary parts of the impedance, ω—angular frequency, and x—the integration variable (0—∞)

A neutral salt spray (NSS) test was used to estimate the barrier properties of the PEO coatings in a corrosive service environment according to the ASTM B117 standard procedure. The test was carried out under continuous spray conditions at temperature of 35 °C, the salt solution used was 5 wt.% NaCl and its pH was around 7.0. The samples were visually inspected after 7 days of salt chamber test duration.

3. Results and Discussion

3.1. Voltage-Time Responses during PEO Process

To investigate the effects of additives used on the nature of processes that occur on the sample surface during the PEO process, changes in the response voltage during the oxidation time were evaluated. Figure 1 shows the voltage-time curves during the PEO process of the samples placed in the Base, BF4, and F electrolytes and the images of the sample in the Base electrolyte at various stages of the PEO process. In all cases, three main stages were identified during the PEO process, which included conventional anodization, spark anodization, and plasma electrolytic oxidation.

During the first stage, a linear increase in voltage is observed within a short period of time, which involves the rapid electrochemical formation of an initial thin oxide film as in the conventional anodization process. The next stage starts when the breakdown voltage is reached, which corresponds to the dielectric breakdown of the oxide film. The breakdown voltages decrease with an increase in the electrolyte conductivity (Table 2). The addition of $NaBF_4$ or NaF to the base electrolyte causes a decrease in the breakdown voltage from 194 to 188 and 177 V, respectively. In this stage, a large number of small white-colored sparks appear, evenly covering the entire surface of the sample. The slope of the voltage-time curves decreases during the spark anodization stage. After about 5 min from the start of the process, the micro-discharges become more intense and their color changes from white to yellow-orange. The essential process of plasma electrolytic oxidation begins, which causes the largest changes in the structure of the coating. The rate of voltage

change decreases as compared to the earlier stage. In the case of the base electrolyte, after 10 min, the voltage increase rate becomes slightly slower than for the other electrolytes and ultimately has the lowest value. The highest final voltage value (421 V) was recorded for the BF4 sample, which was accompanied by the most intense discharges visible on the treated surface. The breakdown and final voltage values for the different electrolytes are listed in Table 4.

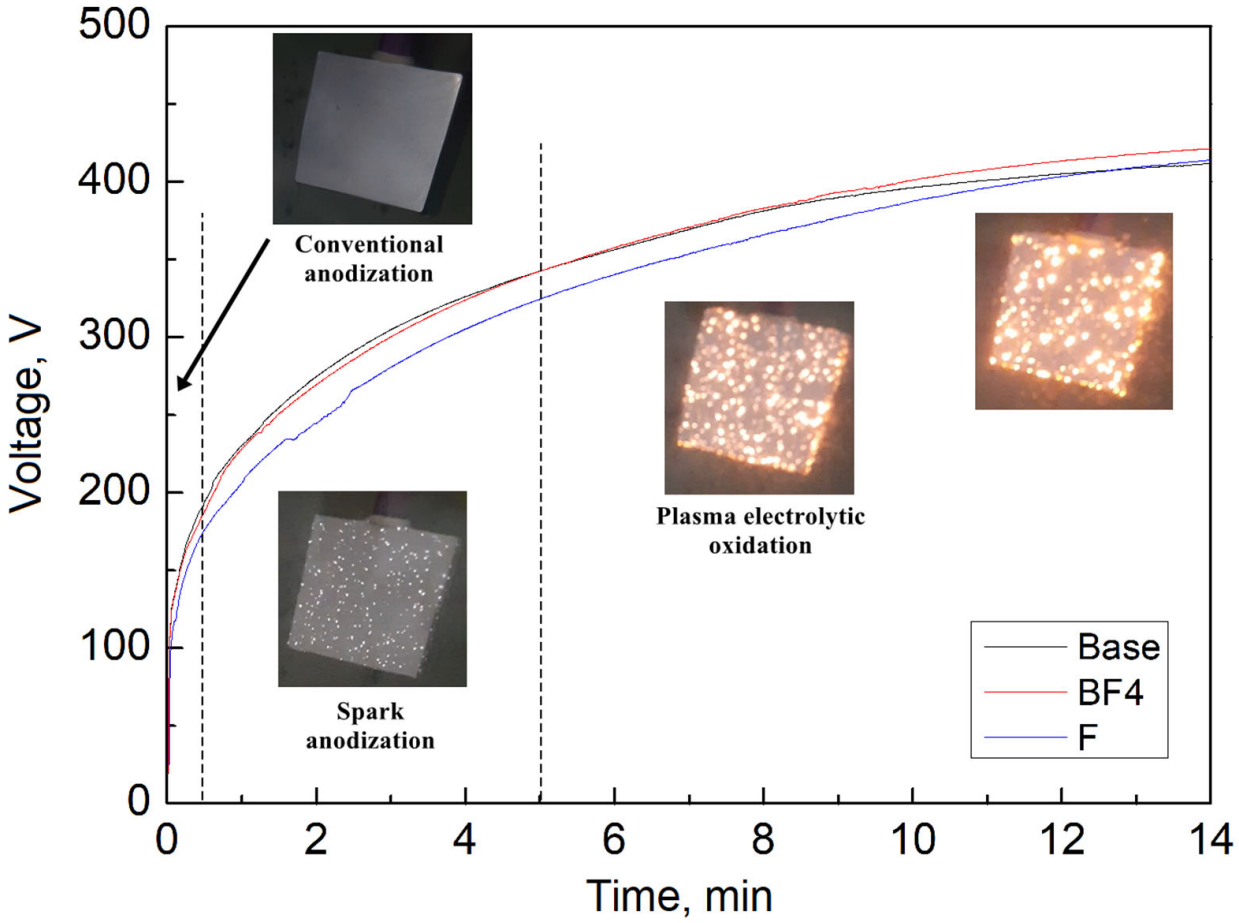

Figure 1. Voltage-time curves during the PEO process in the different electrolytes.

Table 4. The breakdown voltage values and final voltage in the different electrolytes.

Sample Code	Breakdown Voltage, V	Final Voltage, V
Base	194	412
BF4	188	421
F	177	414

3.2. Surface and Cross-Sectional Morphology of PEO Coatings

The SEM images of the surface microstructure and the binary analyzed images of the coatings produced in different electrolytes are shown in Figure 2.

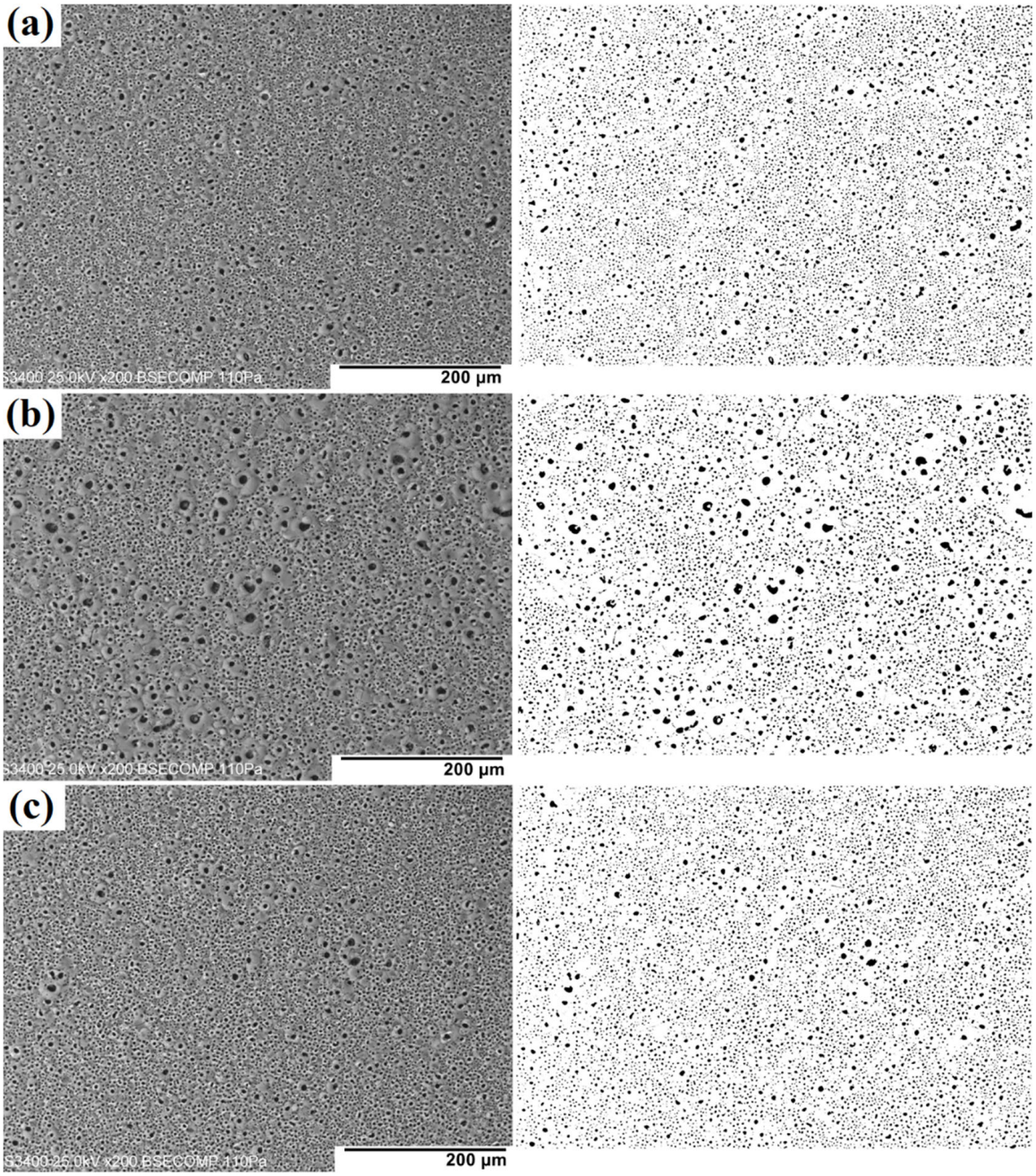

Figure 2. SEM surface morphology and binary analyzed images of the PEO coatings: (**a**) Base; (**b**) BF4; (**c**) F.

The surface of all coatings has a typical crater-like morphology resulting from local microdischarge events that occurred during layer formation in the plasma electrolytic oxidation process. This morphology was created as a result of the outflow of molten material along the microdischarge channel during sparking. The distribution of the outer pore size for all coatings is shown in Figure 3a. In all the cases, the normal distribution was found, which allowed for a Gaussian fit to be determined. Analysis of the SEM images (Figure 2) shows a much greater effect of the addition of $NaBF_4$ on the morphology of the surface, which is related to the presence of large-diameter pores. Therefore, an analysis of the percentage distribution of the outer pore size of PEO coatings anodized in various electrolytes was carried out (Figure 3b). The addition of $NaBF_4$ to the electrolyte was found to cause a threefold increase in the coating surface covered with large pores (with a diameter greater than 5µm, which corresponds with an area greater than about 20 μm^2)

which is almost a quarter of the sample area. The clearly larger outer pore diameter of the BF4 coating is due to the highest value of the final voltage observed during the PEO process, which is caused by the occurrence of electric discharges with the highest power.

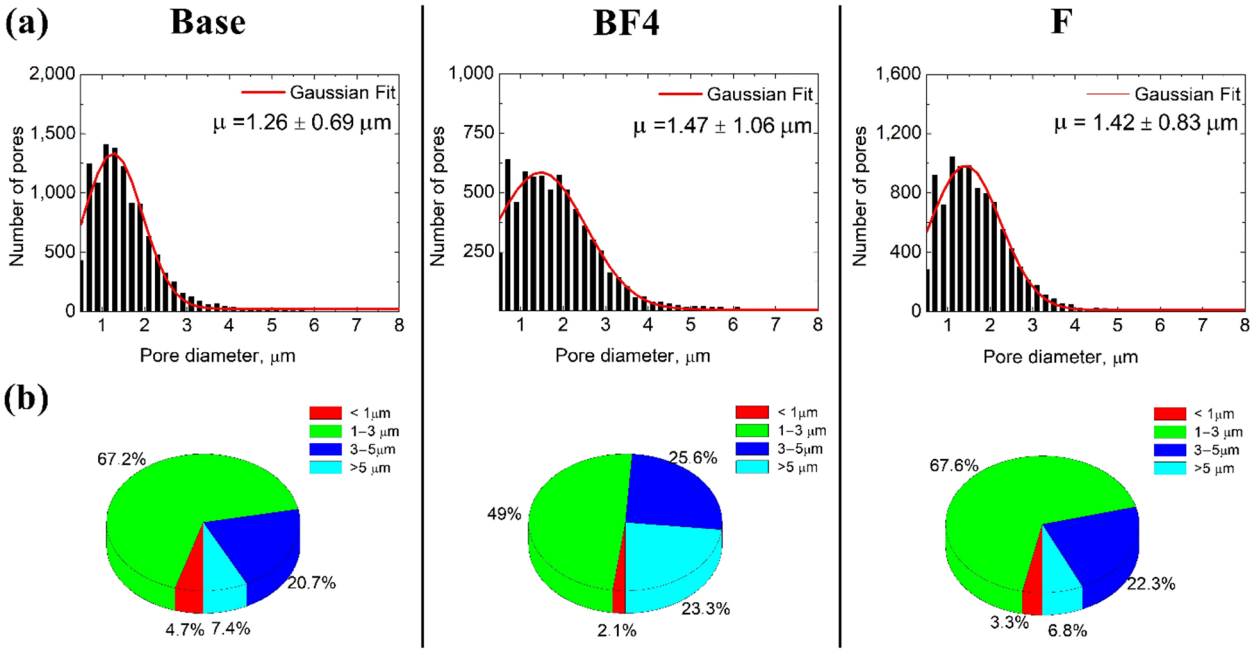

Figure 3. Analysis of the morphology of PEO coatings in various electrolytes: (**a**) pore size distribution; (**b**) percentage pore size distribution.

The morphological characteristics of the PEO coating surface are presented in Table 5. The average total outer porosity (percentage of the area covered by open pores) and the average outer pore diameter (both calculated as the arithmetic average and the mean value of the Gaussian fit) of the BF4 coating are slightly larger compared to other coatings.

Table 5. Morphological characteristics of the surface of PEO coatings.

Sample Code	Average [1] Outer Pore Diameter, μm	Average [2] Outer Pore Diameter, μm	Porosity, %
Base	1.77 ± 2.07	1.26 ± 0.69	9.80
BF4	2.28 ± 2.92	1.47 ± 1.06	10.22
F	1.90 ± 2.08	1.42 ± 0.83	9.72

[1]—the arithmetic average; [2]—the mean value of the Gaussian fit.

The cross-sectional morphology and average thickness of the PEO coatings are shown in Figure 4. As can be seen in the cross-sectional images, in all the cases the structure of the obtained coatings is typical for coatings produced in the PEO process, and two layers exist. The outer layer is relatively thick with visible open and closed pores. The inner layer, close to the metal surface, is very thin but compact and is considered to be the protective layer. The presence of investigated salts in electrolytes causes an increase in the total thickness of the coatings by more than 3 μm (from 9.46 to 12.71 and 12.68 μm for coatings made of solutions containing $NaBF_4$ and NaF, respectively).

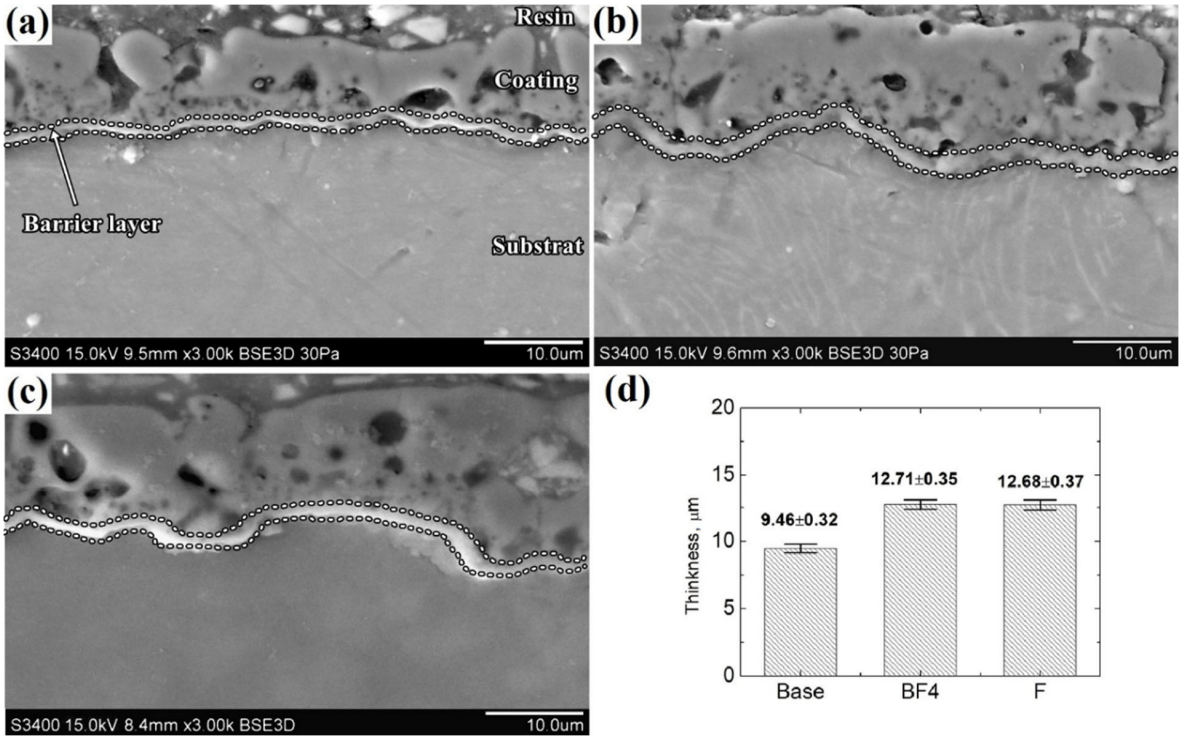

Figure 4. The SEM images of cross-sectional PEO coatings: (**a**) Base; (**b**) BF4; (**c**) F; and (**d**) average values of the thickness of these coatings. (The dashed lines were added to make the inner layer more visible).

3.3. Chemical Composition Analysis of the PEO Coatings

Measurements made on cross-sections of coatings using the EDS analysis have allowed us to determine the chemical composition of the outer and inner layers of coatings obtained in the PEO process (Table 6). The main components of the coatings are magnesium, oxygen, and silicon, which is typical of the conversion coatings formed in silicate electrolytes on magnesium alloys. Moreover, a small amount of aluminum was also found, which is related to its presence in the AZ91D alloy used. In the case of coatings produced in electrolytes containing $NaBF_4$ and NaF, fluorine was also incorporated into the coatings. Analyzing the content of individual elements in the outer and inner layers, it can be seen that the amounts of Mg and Al (coming from the alloy) are greater in the inner (barrier) layer, while the amounts of O and Si (coming from the electrolyte) are greater in the outer layer. In the case of fluoride ions, despite the fact that they come from the electrolyte, their higher content was recorded in the inner layer, which has already been described [20,27]. The distribution of chemical elements across the PEO coating obtained with the addition of $NaBF_4$ is shown in Figure 5. Elemental maps of the BF4 coating confirmed an increase in the amount of fluoride in the barrier layer.

Table 6. Elemental contents (in atomic percentage) determined by EDS for the coatings obtained in different electrolytes.

Sample Code	Layer	Elements Content, at.%				
		Mg	O	Si	Al	F
Base	outer	37.4	43.0	14.9	4.6	0.0
	inner	48.8	37.2	8.2	5.7	0.0
BF4	outer	36.9	42.9	13.9	3.8	2.4
	inner	47.2	32.6	7.7	5.0	7.4
F	outer	33.3	45.5	15.7	3.5	1.9
	inner	44.6	38.1	6.2	4.2	6.8

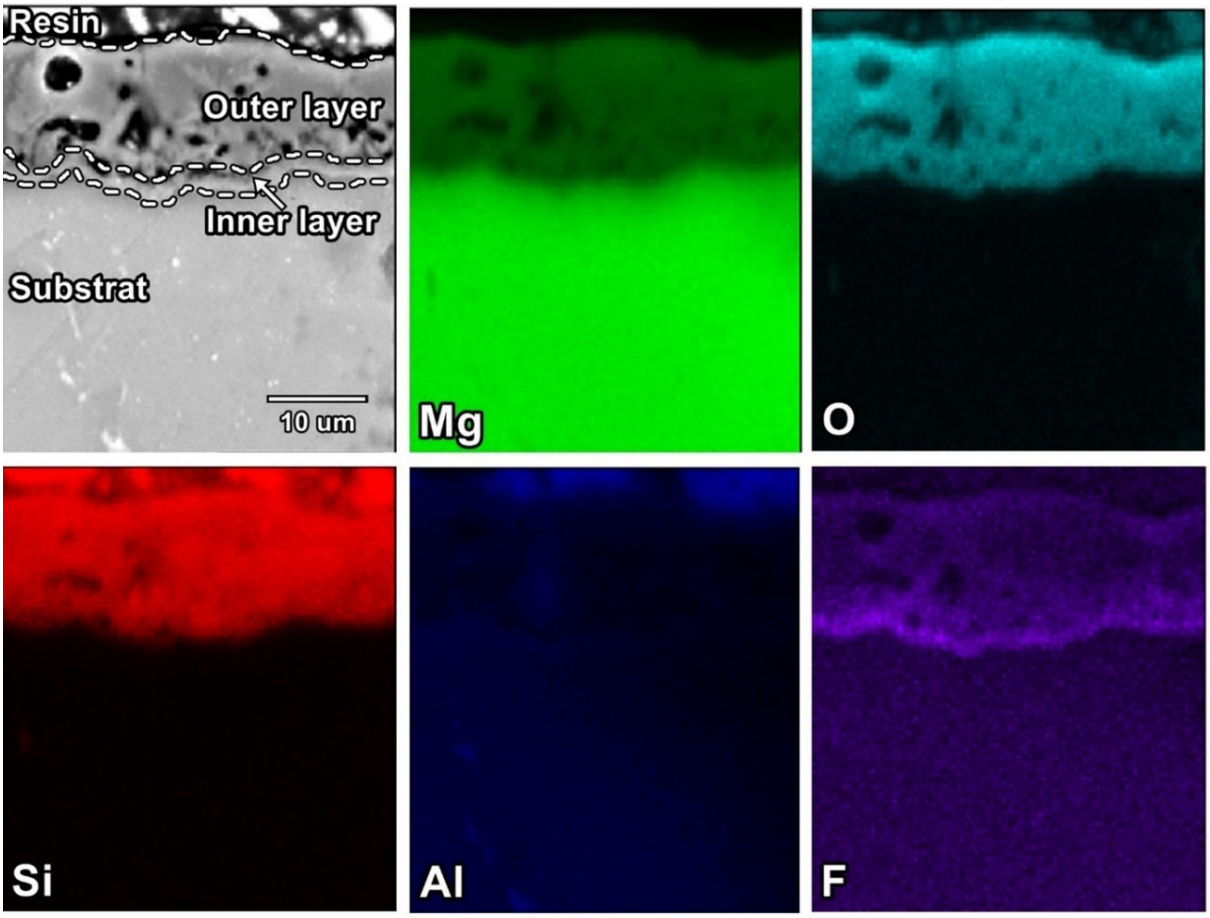

Figure 5. Microstructure and elemental distribution in the cross-section of the BF4 coating.

The XPS study was performed to obtain more information about the composition of the coatings. The XPS survey spectrum of the investigated coatings (outer layer) is presented in Figure 6a. All coatings have shown very similar spectra, which indicated the presence of mainly magnesium, oxygen, and silicon. When $NaBF_4$ or NaF was present in the electrolyte, fluorine is also incorporated into the coatings. Figure 6b presents the specific spectra of F 1s, which correspond to MgF_2 (685.7 eV).

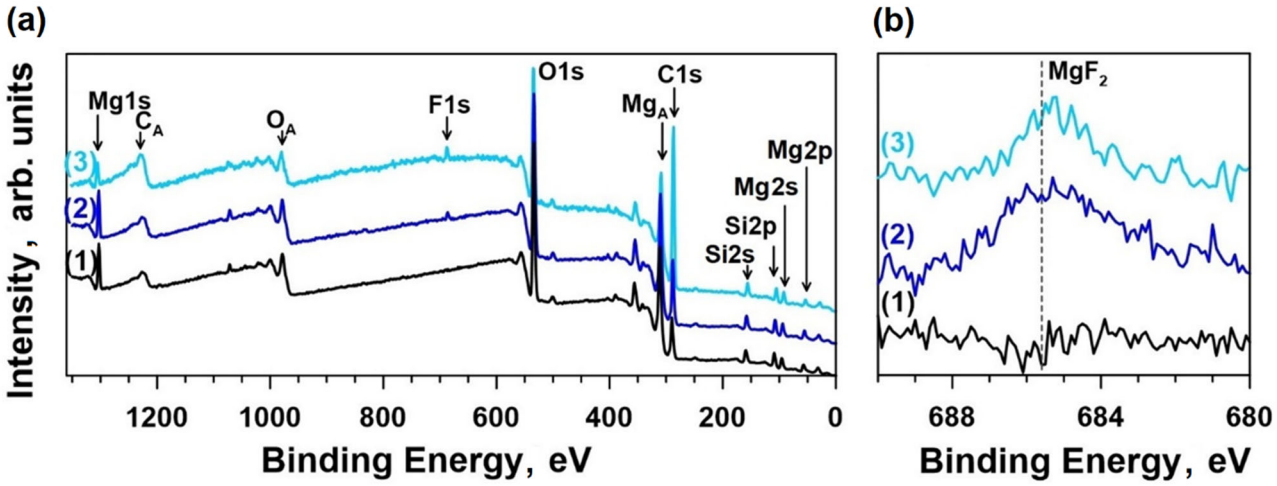

Figure 6. XPS spectra of PEO coatings: (**a**) survey spectrum; (**b**) specific spectrum of F 1s (1—Base, 2—F, 3—BF4).

A detailed analysis of the chemical composition of the BF4 coating at different depths is shown in Figure 7. The presented data indicate the composition changes along the cross-section of the coating, and these changes are particularly significant in the barrier layer.

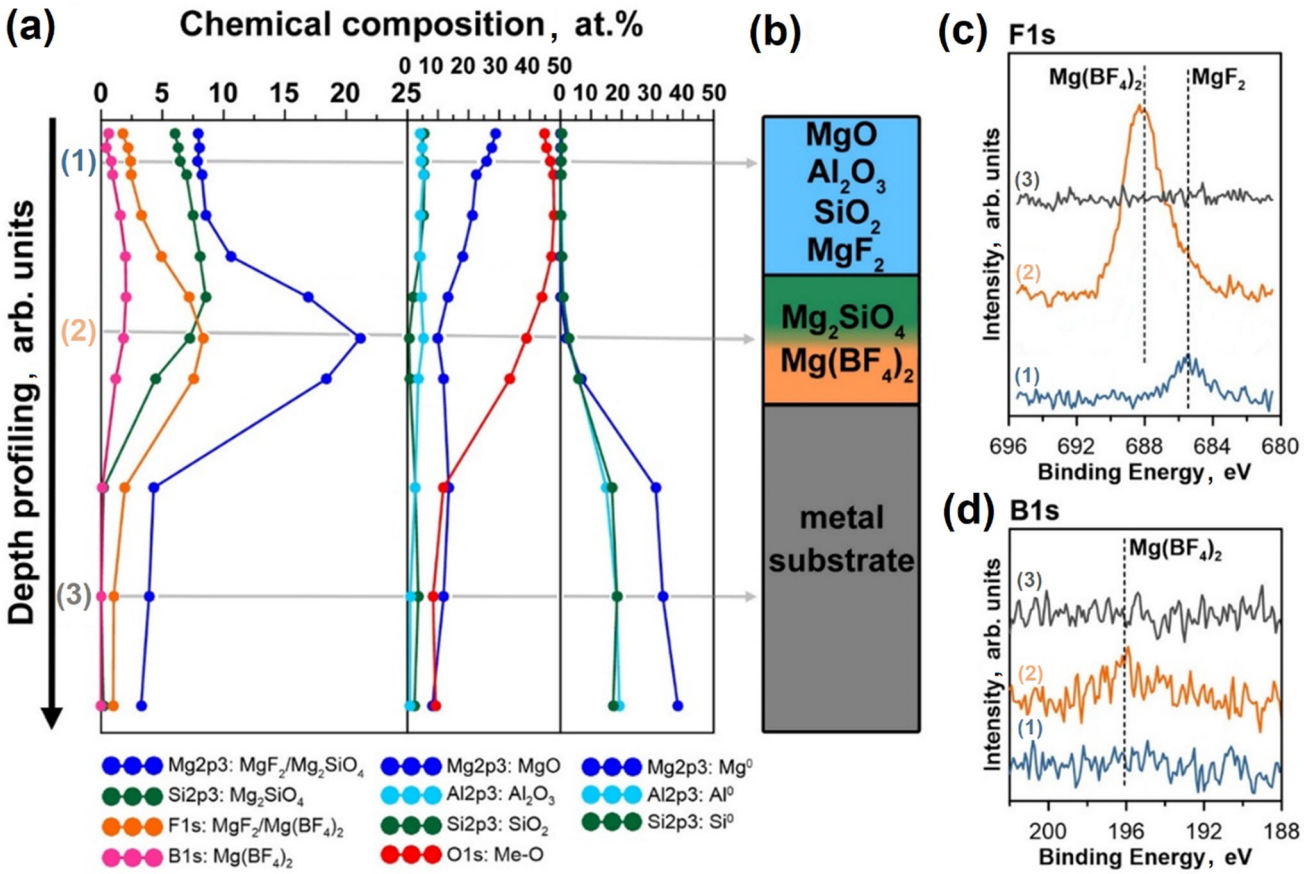

Figure 7. XPS analysis of the BF4 coating: (**a**) the chemical composition of the depth profile; (**b**) the cross-section scheme; (**c**) specific spectra of fluorine (F 1s) and (**d**) boron (B 1s) at the outer layer (point 1); inner layer (point 2); and metal substrate (point 3).

The XPS analysis has shown that in the outer layer (point 1), the dominant components of the coating are simple compounds, mainly MgO. In the inner layer (point 2), a clear decrease in the intensity of the Mg 2p3 and Si 2p3 signals derived from MgO and SiO_2, respectively, is observed, accompanied by an increase in the characteristic signals of a more complex Mg_2SiO_4 compound. In the inner layer, an increase in the intensity of the fluorine (F 1s) and boron (B 1s) signals is also visible. Analyzing the fluorine spectra (Figure 7c), the shift of the peak F 1s' maximum is visible from the value of 685.4 eV (characteristic of MgF_2) in the outer layer to 687.9 eV in the inner layer, which suggests the formation of a more complex fluorine compound, probably Mg $(BF_4)_2$, close to the substrate material. In the literature, there are no XPS data available for Mg $(BF_4)_2$. However, the energy value of the peak F 1s for $NaBF_4$ is equal to 687.0 eV [44], which is close to the observed value of the shifted peak. Moreover, the possibility of the formation of a boron compound in the form of tetrafluoroborate is supported by the high energy for the peak B 1s (196.1 eV) in the barrier layer (Figure 7d). The values of B 1s' peak for $NaBF_4$ (195.8 eV), KBF_4 (195.6 eV), and NH_4BF_4 (194.9 eV) are higher than the values for B_2O_3 (B 1s 192.0–193.7 eV) [44]. The possibility of the occurrence of BF_4^- in the inner layer is also supported by the relative content of B and F (at.%), which is approximately 1:4.

Analyzing the results obtained and taking into account literature data on the composition of this type of coating, the occurrence of the following reactions is proposed.

$$Mg^0 \rightarrow Mg^{2+} + 2e^- \quad (5)$$

$$Mg^{2+} + 2OH^- \rightarrow Mg(OH)_2 \rightarrow MgO \quad (6)$$

$$2Mg^{2+} + SiO_3^{2-} + 2OH^- \rightarrow Mg_2SiO_4 + H_2O \quad (7)$$

$$SiO_3^{2-} \rightarrow SiO_2 + \frac{1}{2} O_2 + 2e^- \quad (8)$$

$$2MgO + SiO_2 \rightarrow Mg_2SiO_4 \quad (9)$$

$$Mg^{2+} + 2F^- \rightarrow MgF_2 \quad (10)$$

$$BF_4^- + 3OH^- \rightarrow B(OH)_3 + 4F^- \quad (11)$$

$$Mg^{2+} + BF_4^- \rightarrow Mg(BF_4)_2 \quad (12)$$

The metallic magnesium of the base material is oxidized to form Mg^{2+} (Equation (5)), which then reacts with hydroxyl ions to form $Mg(OH)_2$. As a result of the high temperature in the plasma discharge channel, the hydroxide is converted to an oxide (Equation (6)). Furthermore, magnesium ions in an alkaline environment can react with metasilicate ions to form forsterite (Mg_2SiO_4) (Equation (7)) [45–47]. In the process of plasma oxidation, direct oxidation of metasilicate ions can also occur and SiO_2 is formed (Equation (8)) [48,49]. Silicon oxide with magnesium oxide at high temperature can also form forsterite (Equation (9)) [49,50]. As a result of the above reactions, the conversion coating formed is mainly composed of MgO and Mg_2SiO_4. Due to the presence of aluminum in the magnesium alloy (AZ91D), this element is also incorporated in a small amount into the formed layer, most likely in the form of Al_2O_3 [32,51] and $MgAl_2O_4$ [25,52].

In the case of the coating formed in an electrolytic bath containing NaF, the fluoride ion combines with Mg^{2+} to form MgF_2 (Equation (10)) [25]. We have also found that in the presence of $NaBF_4$ in the baths, MgF_2 appears in the outer layer, which is caused by the partial decomposition of the BF_4^- ion in an alkaline environment (Equation (11)). However, in the inner layer of this coating, the main fluorine-containing compound is $Mg(BF_4)_2$ (Equation (12)), which is indicated by the shift of F 1s peak maximum in the XPS spectra and also by the relative content of B and F (at.%), which is approximately 1:4 (Figure 7a).

In the literature data, there have been no reports so far that in the presence of complex fluorine ions in the electrolyte, the complex ions are incorporated into the formed layer. When Na_3AlF_6 [31] was present in the electrolyte, it was suggested that hydrolysis of the compound to $Al(OH)_3$ and the release of F^- ions occurred, and fluorine was incorporated into the layer in the form of MgF_2. Aluminum hydroxide under the conditions of plasma oxidation was transformed into Al_2O_3. In the case of K_2ZrF_6 [28], the formation of zirconium oxide and the release of fluoride ions in an alkaline environment have been proposed. In the presence of Na_2SiF_6 [30], the proposed mechanism involves the decomposition of SiF_6^- and the formation of MgF_2 and Mg_2SiO_4. When K_2TiF_6 was used [29], its hydrolysis of $Ti(OH)_4$ was suggested, which caused the formation of Mg_2TiO_4 in the formed coating.

3.4. Corrosion Resistance of PEO Coatings

Potentiodynamic polarization (PDP) tests were carried out to establish the anticorrosive properties of the investigated coatings. The results are shown in Figure 8. The corresponding parameters are listed in Table 7.

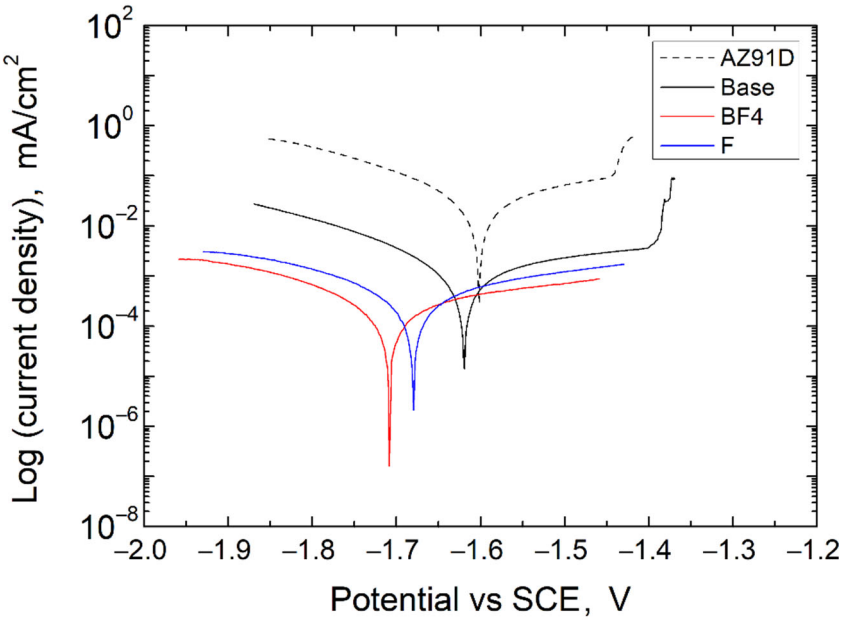

Figure 8. Potentiodynamic polarization curves of the uncoated AZ91D Mg alloy and the samples with coatings formed in the PEO process.

Table 7. Potentiodynamic polarization parameters of the uncoated AZ91D Mg alloy and the samples with coatings formed in the PEO process.

Sample Code	E_{CORR} *vs.* SCE, V	j_{CORR}, μA/cm^2	β_A, mV/dec	β_C, mV/dec	R_P,kΩ·cm^2	F
AZ91D	−1.60	29.8	307	178	1.65	
Base	−1.62	1.20	402	180	45.01	3.20×10^{-2}
BF4	−1.71	0.26	478	242	265.9	2.76×10^{-3}
F	−1.68	0.45	431	250	152.7	5.93×10^{-3}

The results obtained show that all of the PEO-coated samples exhibit improved corrosion performance compared to the untreated magnesium alloy. The presence of fluorine-containing compounds in the basic silicate bath further increases the anticorrosive properties, including the disappearance of the pitting potential in the PDP curves in the scanning range used. The formation of the conversion coatings on the magnesium alloy shifts the corrosion potential toward more negative values. However, the corrosion rate is proportional to the corrosion current. The value of the corrosion current density (j_{CORR}) decreased from 29.8 μA/cm^2 for the uncoated AZ91D Mg alloy to 1.20, 0.45, and 0.26 μA/cm^2 for the Base, F, and BF4 coatings, respectively. Polarization resistance (R_P) values for the investigated samples increase in the order AZ91D < Base < F < BF4. The lowest value of porosity (F), calculated on the basis of electrochemical measurements, for the BF4 sample proves the highest tightness of the formed coating. These results are in contrast to the results of the outer porosity measurements based on the analysis of the SEM measurements (Figure 2). This indicates that the key factor influencing the corrosion resistance of conversion coatings produced in the PEO process is the inner layer, which for the BF4 sample is homogeneous and compact (Figure 4), and despite the larger size of the open pores in the outer layer, this coating shows the best protection properties in the corrosive environment among the tested samples.

Electrochemical impedance spectroscopy (EIS) studies were carried out after 3 h of immersion in SBF solution to analyze the corrosion mechanism of the PEO coatings. The EIS results in the form of the Nyquist and Bode plots are presented in Figure 9. To obtain the best fit of the test data with the lowest possible error, different equivalent circuits were analyzed, taking into account the physical model of the conversion coating and the

corrosion processes occurring. Selected models of the equivalent circuits for uncoated AZ91D alloy and PEO coatings that allowed good fits of the experimental data were presented in Figure 10.

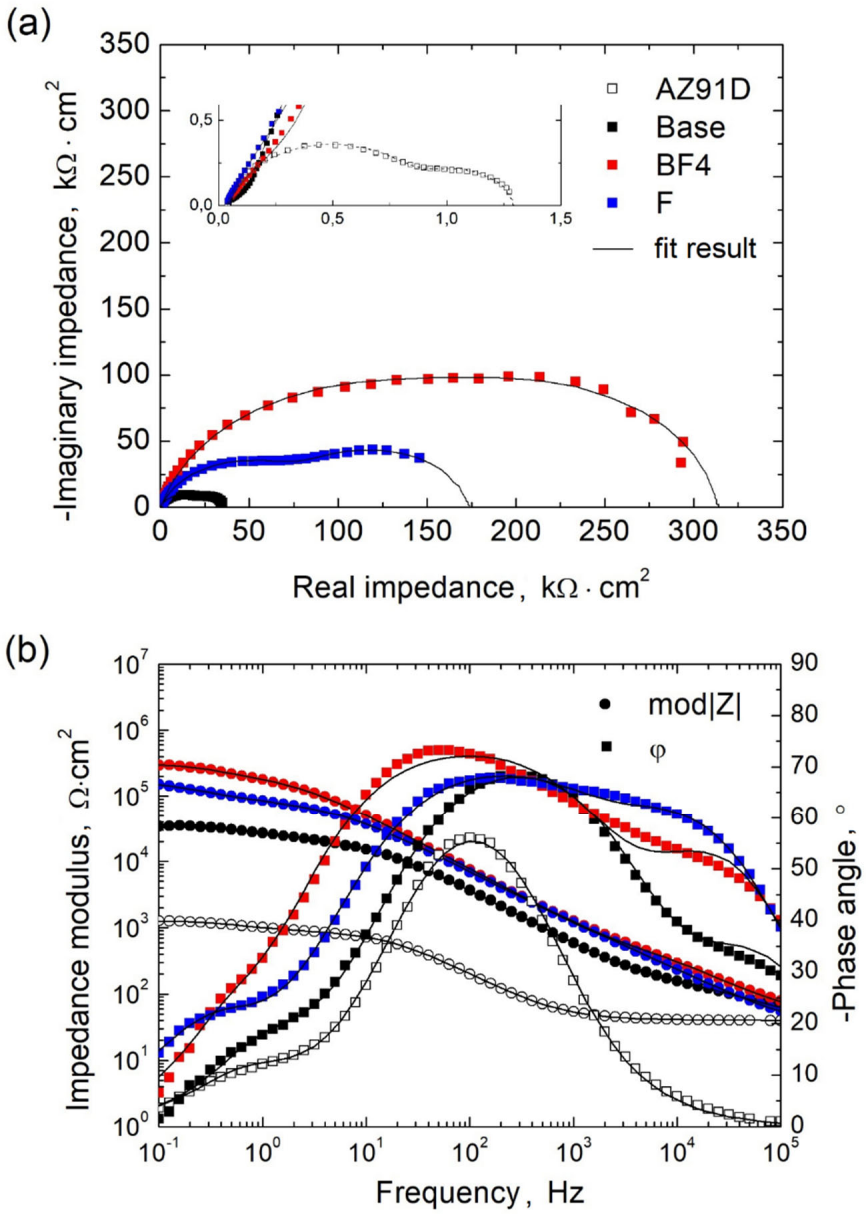

Figure 9. Results of EIS measurements for the uncoated AZ91D Mg alloy and the PEO treated samples in different electrolytes: (**a**) Nyquist; (**b**) Bode plots.

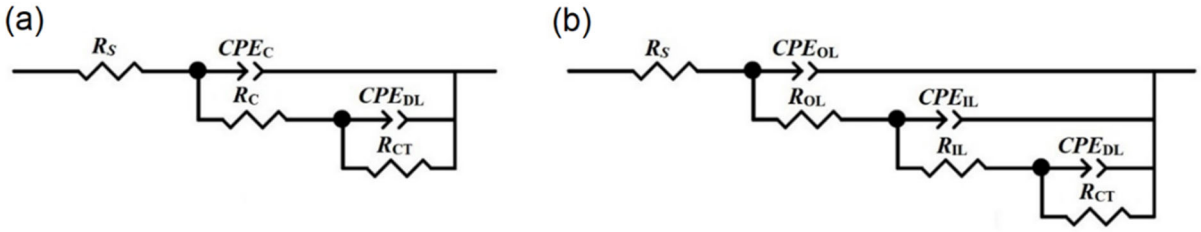

Figure 10. Equivalent circuits used to fit data of EIS measurements: (**a**) uncoated AZ91D Mg alloy; (**b**) PEO-treated samples.

In the proposed circuits, R_S stands for electrolyte resistance of the electrolyte between the working and reference electrodes. Two consecutive groups of paralleled combinations of resistors (R_{OL} and R_{IL}) and constant phase elements (CPE_{OL} and CPE_{IL}) were applied to describe the resistance and capacitance of the outer porous layer and inner barrier layer, respectively. The outer porous layer of the coating is responsible for the high-frequency relaxation process (10^4–10^5 Hz), while the middle frequency response of the system (10^1–10^3 Hz) can be attributed to the inner barrier layer. R_{CT} and CPE_{DL} represent the resistance of charge transfer and the electrochemical double-layer capacitor at the substrate/coating interface, which corresponds to the low-frequency time constant (1 to 0.1 Hz) [40,53]. In the case of the model describing the corrosion of uncoated AZ91D alloy, only two time constants are present, the one at higher frequencies corresponding to the self-formed oxide film on magnesium alloy in an aqueous solution (R_C and CPE_C). The second at lower frequencies can be assigned to the corrosion processes of the magnesium alloy (R_{CT}, CPE_{DL}) [54]. The constant phase elements (*CPE*s) used in equivalent circuits were selected instead of pure capacitance for better fitting because the conversion coating surface is physicochemically inhomogeneous, uneven, and rough. The *CPE* impedance is described as:

$$Z_{CPE} = \frac{1}{Q(j\omega)^n} \quad (13)$$

where Q is the constant admittance, j is an imaginary number, and ω is the angular frequency. The number n is an empirical exponent, whose value is equal to 1 for a perfect capacitor and equal to 0 for a perfect resistor.

The simulated values (fitting parameters) obtained by matching the theoretical model and experimental data are presented in Tables 8 and 9 for the uncoated AZ91D Mg alloy and PEO-treated samples, respectively. The chi-square values for the fitted curves of all samples were in the range of 10^{-3}–10^{-4}. For the equivalent circuit of PEO coatings, the total resistance (R_{TOTAL}) is calculated as shown in Equation (14):

$$R_{TOTAL} = R_{OL} + R_{IL} + R_{CT} \quad (14)$$

Table 8. Equivalent circuit parameters obtained from the fitting of the EIS experimental data for the uncoated AZ91D Mg alloy.

Sample Code	R_S, Ω·cm²	CPE_C, μS·sec^n/cm²	n_C	R_C, Ω·cm²	CPE_{DL}, μS·sec^n/cm²	n_{DL}	R_{CT}, Ω·cm²	R_{TOTAL}, kΩ·cm²
AZ91D	40	20.1	0.860	891	896	0.894	364	1.26

Table 9. Equivalent circuit parameters obtained from the fitting of the EIS experimental data for the PEO-treated samples.

Sample Code	R_S, Ω·cm²	CPE_{OL}, μS·sec^n/cm²	n_{OL}	R_{OL}, kΩ·cm²	CPE_{IL}, μS·sec^n/cm²	n_{IL}	R_{IL}, kΩ·cm²	CPE_{DL}, μS·sec^n/cm²	n_{DL}	R_{CT}, kΩ·cm²	R_{TOTAL}, kΩ·cm²
Base	39	0.651	0.787	0.172	0.604	0.864	23.3	20.6	0.844	13.2	36.67
BF4	44	0.325	0.823	0.892	0.246	0.861	235.0	5.04	1.000	78.1	313.99
F	32	0.589	0.805	2.350	0.176	0.826	89.5	9.87	0.869	82.0	173.85

The EIS results confirm the positive effect of the conversion coatings produced in the PEO process on the anticorrosive properties of the AZ91D alloy (R_{TOTAL} 1.26 kΩ·cm²). The total coating resistance increases from 36.67 kΩ·cm² for the coating produced in the base electrolyte to approximately 174 and 314 kΩ·cm² for samples F and BF4, respectively.

In all of the investigated coatings, the calculated impedance of the inner layer (R_{IL}) is much higher than the other resistance elements that describe the coatings, indicating that the inner layer plays a crucial role in corrosion resistance. For the coating produced in the

electrolyte containing $NaBF_4$, this value is the highest (235 kΩ·cm^2). It should be noted that the total impedance value of the investigated coatings is also significantly influenced by the ongoing corrosion processes (R_{CT}). In the case of a coating produced in the electrolyte containing NaF, the value is comparable to the value of the inner layer resistance. The outer layer has the least influence on the barrier properties, which is caused by its high porosity. Nevertheless, the open pores present on the surface of PEO coatings make them a good base for the use of topcoat layers by increasing their adhesion.

The Kramers–Kronig transformations were used to evaluate the quality of the EIS data. Typical K–K transformations of impedance data obtained in the present study are shown in Figure 11 (the real to imaginary impedance and the imaginary to real impedance transformations).

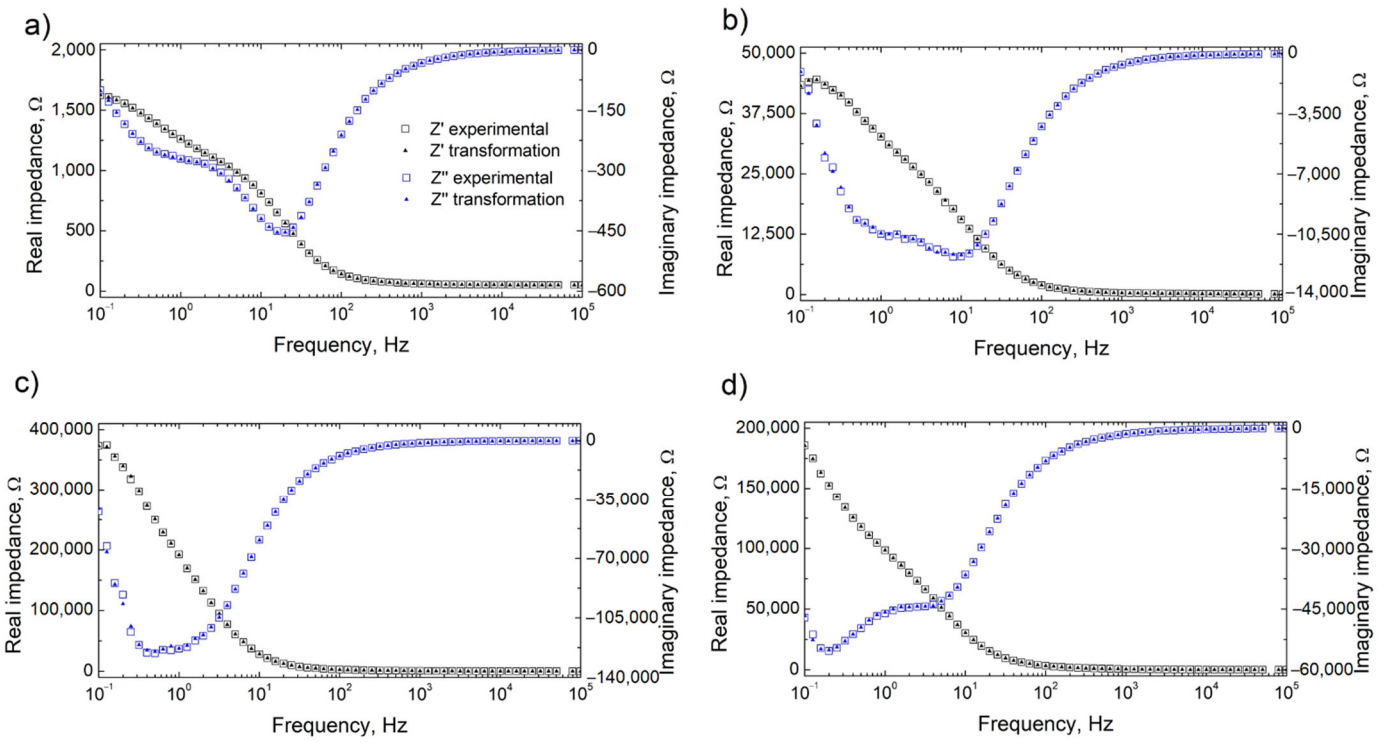

Figure 11. Comparison of experimental impedance data and transformed impedance data using K–K relationships: (**a**) uncoated AZ91D Mg alloy; (**b**) Base; (**c**) BF4; (**d**) F—PEO coatings.

The transformation results for all PEO coatings correspond well with the measured data both real and imaginary components obey the Kramers–Kronig relations.

To verify the anticorrosive properties of the coated surfaces investigated, a salt chamber test was performed. Figure 12 shows the macroscopic appearance of the samples after the neutral salt spray test in 5 wt.% NaCl for 168 h.

The coating formed in the base electrolyte had many small pits throughout the surface and large local white areas made of the resulting corrosion products. The introduction of NaF to the bath resulted in the disappearance of visible signs of pitting corrosion and a reduction in the number of areas with solid corrosion products. The replacement of NaF with $NaBF_4$ in the PEO bath caused a further reduction in the number of visible corrosion spots. The appearance of the samples after the salt spray test confirms the results obtained by electrochemical measurements in the SBF solution. The presence of fluoride ions in the PEO bath improves the anticorrosion properties of the conversion layers produced. The best results were obtained for the BF4 coating.

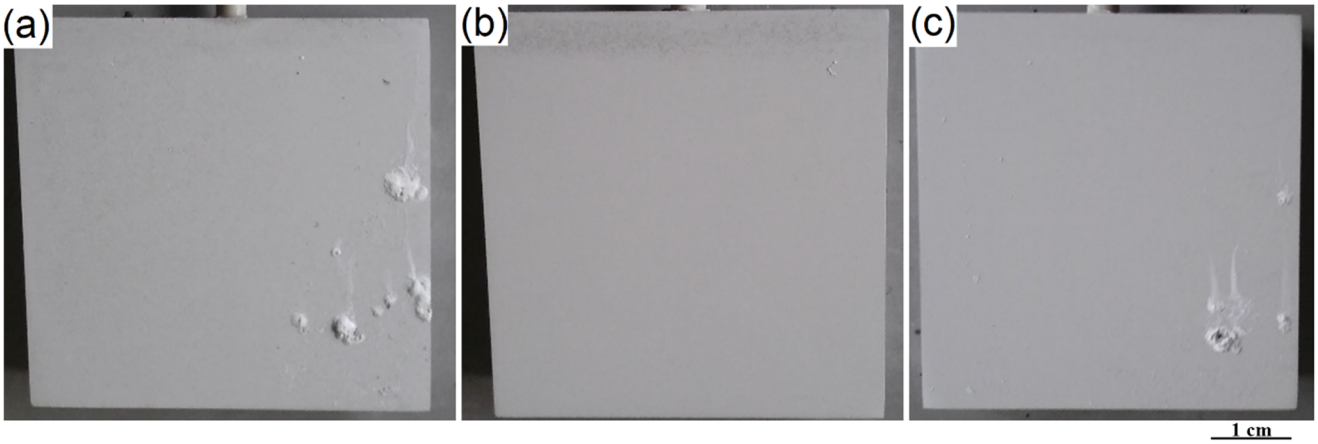

Figure 12. Images of the PEO coatings surface: (**a**) Base; (**b**) BF4; (**c**) F, after neutral salt spray test in 5 wt.% NaCl for 168 h.

4. Conclusions

In the presented study, the PEO coatings produced on the AZ91D Mg alloy in alkaline silicate baths with the addition of NaF or $NaBF_4$ were examined. The results obtained can be summarized as follows:

- The presence of both fluorine-containing salts in the electrolyte bath enhances the performance of the coatings produced. These coatings are thicker and show increased resistance to corrosion. However, the best barrier properties have been observed for the coating obtained from the electrolyte containing sodium tetrafluoroborate.
- Fluorine is present mainly in the inner layer. XPS studies have shown that $Mg(BF_4)_2$ occurs in the inner layer when the electrolyte bath contains sodium tetrafluoroborate and its presence is responsible for the best properties of the coatings.
- The use of sodium tetrafluoroborate in the electrolyte bath causes a visible increase in the diameter of the pores in the outer layer of the coating. However, this can be useful in increasing the adhesion of the topcoat layers.

5. Patents

- The US 11001927B2 patent has been granted from the work reported in this manuscript.

Author Contributions: Ł.F.: conceptualization, methodology, data curation, writing—original draft, formal analysis, investigation, validation, visualization. G.N.: conceptualization, funding acquisition, writing—review & editing. K.D.: writing—review & editing. J.R., M.W.: data curation, formal analysis, investigation. J.S.: conceptualization, funding acquisition, writing—review & editing. K.R.: project administration, funding acquisition, resources. A.S.: conceptualization, validation, supervision, writing—review & editing. All authors have read and agreed to the published version of the manuscript.

Funding: This research was funded by the National Centre for Research and Development (Poland) under Grant No. PBS1/B5/5/2012.

Institutional Review Board Statement: Not applicable.

Informed Consent Statement: Not applicable.

Data Availability Statement: Data are available on request from the authors.

Conflicts of Interest: The authors declare no conflict of interest.

References

1. Gray, J.E.; Luan, B. Protective coatings on magnesium and its alloys—A critical review. *J. Alloys Compd.* **2002**, *336*, 88–113. [CrossRef]

2. El Mahallawy, N.A.; Shoeib, M.A.; Abouelenain, M.H. AZ91 magnesium alloys: Anodizing of using environmental friendly electrolytes. *J. Surf. Eng. Mater. Adv. Technol.* **2011**, *1*, 62–72. [CrossRef]
3. Gerengi, H.; Cabrini, M.; Solomon, M.M.; Kaya, E. Understanding the corrosion behavior of the AZ91D alloy in simulated body fluid through the use of dynamic EIS. *ACS Omega* **2022**, *7*, 11929–11938. [CrossRef]
4. Wu, C.-Y.; Zhang, J. State-of-art on corrosion and protection of magnesium alloys based on patent literatures. *Trans. Nonferrous Met. Soc. China* **2011**, *21*, 892–902. [CrossRef]
5. Zhang, D.; Peng, F.; Liu, X. Protection of magnesium alloys: From physical barrier coating to smart self-healing coating. *J. Alloys Compd.* **2021**, *853*, 157010. [CrossRef]
6. Chang, S.-H.; Niu, L.; Su, Y.; Wang, W.; Tong, X.; Li, G. Effect of the pretreatment of silicone penetrant on the performance of the chromium-free chemfilm coated on AZ91D magnesium alloys. *Mater. Chem. Phys.* **2016**, *171*, 312–317. [CrossRef]
7. Amiri, H.; Mohammadi, I.; Afshar, A. Electrophoretic deposition of nano-zirconia coating on AZ91D magnesium alloy for bio-corrosion control purposes. *Surf. Coat. Technol.* **2017**, *311*, 182–190. [CrossRef]
8. Kavitha, R.J.; Ravichandran, K.; Sankara Narayanan, T.S.N. Deposition of strontium phosphate coatings on magnesium by hydrothermal treatment: Characteristics, corrosion resistance and bioactivity. *J. Alloys Compd.* **2018**, *745*, 725–743. [CrossRef]
9. Kuo, Y.-L.; Chang, K.-H. Atmospheric pressure plasma enhanced chemical vapor deposition of SiOx films for improved corrosion resistant properties of AZ31 magnesium alloys. *Surf. Coat. Technol.* **2015**, *283*, 194–200. [CrossRef]
10. Li, Q.; Zhang, Q.; An, M. Enhanced corrosion and wear resistance of AZ31 magnesium alloy in simulated body fluid via electrodeposition of nanocrystalline zinc. *Materialia* **2018**, *4*, 282–286. [CrossRef]
11. Harada, Y.; Kumai, S. Effect of ceramics coating using sol–gel processing on corrosion resistance and age hardening of AZ80 magnesium alloy substrate. *Surf. Coat. Technol.* **2013**, *228*, 59–67. [CrossRef]
12. Hu, R.-G.; Zhang, S.; Bu, J.-F.; Lin, C.-J.; Song, G.-L. Recent progress in corrosion protection of magnesium alloys by organic coatings. *Prog. Org. Coat.* **2012**, *73*, 129–141. [CrossRef]
13. Yerokhin, A.L.; Nie, X.; Leyland, A.; Matthews, A.; Dowey, S.J. Plasma electrolysis for surface engineering. *Surf. Coat. Technol.* **1999**, *122*, 73–93. [CrossRef]
14. Hussein, R.O.; Nie, X.; Northwood, D.O. An investigation of ceramic coating growth mechanisms in plasma electrolytic oxidation (PEO) processing. *Electrochim. Acta* **2013**, *112*, 111–119. [CrossRef]
15. Florczak, Ł.; Nawrat, G.; Kwolek, P.; Sieniawski, J.; Sobkowiak, A. Plazmowe utlenianie elektrolityczne jako metoda ochrony przed korozją magnezu i jego stopów / Plasma electrolytic oxidation as a method for protection against corrosion of magnesium and its alloys. *Przemysł Chem.* **2018**, *97*, 2145–2153. [CrossRef]
16. Clyne, T.W.; Troughton, S.C. A review of recent work on discharge characteristics during plasma electrolytic oxidation of various metals. *Int. Mater. Rev.* **2019**, *64*, 127–162. [CrossRef]
17. Sikdar, S.; Menezes, P.V.; Maccione, R.; Jacob, T.; Menezes, P.L. Plasma electrolytic oxidation (PEO) process-processing, properties, and applications. *Nanomaterials* **2021**, *11*, 1375. [CrossRef] [PubMed]
18. Yao, W.; Wu, L.; Wang, J.; Jiang, B.; Zhang, D.; Serdechnova, M.; Shulha, T.; Blawert, C.; Zheludkevich, M.L.; Pan, F. Micro-arc oxidation of magnesium alloys: A review. *J. Mater. Sci. Technol.* **2022**, *118*, 158–180. [CrossRef]
19. Barati Darband, G.; Aliofkhazraei, M.; Hamghalam, P.; Valizade, N. Plasma electrolytic oxidation of magnesium and its alloys: Mechanism, properties and applications. *J. Magnes. Alloy.* **2017**, *5*, 74–132. [CrossRef]
20. Gnedenkov, S.V.; Khrisanfova, O.A.; Zavidnaya, A.G.; Sinebryukhov, S.L.; Egorkin, V.S.; Nistratova, M.V.; Yerokhin, A.; Matthews, A. PEO coatings obtained on an Mg–Mn type alloy under unipolar and bipolar modes in silicate-containing electrolytes. *Surf. Coat. Technol.* **2010**, *204*, 2316–2322. [CrossRef]
21. Chen, Y.; Yang, Y.; Zhang, T.; Zhang, W.; Wang, F.; Lu , X.; Blawert, C.; Zheludkevich, M.L. Interaction effect between different constituents in silicate-containing electrolyte on PEO coatings on Mg alloy. *Surf. Coat. Technol.* **2016**, *307*, 825–836. [CrossRef]
22. Chen, Y.; Yang, Y.; Zhang, W.; Zhang, T.; Wang, F. Influence of second phase on corrosion performance and formation mechanism of PEO coating on AZ91 Mg alloy. *J. Alloys Compd.* **2017**, *718*, 92–103. [CrossRef]
23. Gawel, L.; Nieuzyla, L.; Nawrat, G.; Darowicki, K.; Slepski, P. Impedance monitoring of corrosion degradation of plasma electrolytic oxidation coatings (PEO) on magnesium alloy. *J. Alloys Compd.* **2017**, *722*, 406–413. [CrossRef]
24. Liang, J.; Guo, B.; Tian, J.; Liu, H.; Zhou, J.; Xu, T. Effect of potassium fluoride in electrolytic solution on the structure and properties of microarc oxidation coatings on magnesium alloy. *Appl. Surf. Sci.* **2005**, *252*, 345–351. [CrossRef]
25. Wang, L.; Chen, L.; Yan, Z.; Wang, H.; Peng, J. Effect of potassium fluoride on structure and corrosion resistance of plasma electrolytic oxidation films formed on AZ31 magnesium alloy. *J. Alloys Compd.* **2009**, *480*, 469–474. [CrossRef]
26. Nawrat, G.; Wierzbińska, M.; Misztal, A.; Gonet, M.; Lach, G.; Nieużyła, Ł.; Koszorek, A. Elektrolityczne utlenianie plazmowe stopu magnezu AZ91D / Plasma electrolytic oxidation of magnesium alloy AZ91D. *Ochr. Przed Korozją* **2017**, *60*, 131–135. [CrossRef]
27. Mingo, B.; Arrabal, R.; Mohedano, M.; Llamazares, Y.; Matykina, E.; Yerokhin, A.; Pardo, A. Influence of sealing post-treatments on the corrosion resistance of PEO coated AZ91 magnesium alloy. *Appl. Surf. Sci.* **2018**, *433*, 653–667. [CrossRef]
28. Rehman, Z.U.; Shin, S.H.; Hussain, I.; Koo, B.H. Structure and corrosion properties of the two-step PEO coatings formed on AZ91D Mg alloy in K_2ZrF_6-based electrolyte solution. *Surf. Coat. Technol.* **2016**, *307*, 484–490. [CrossRef]
29. Tang, M.; Feng, Z.; Li, G.; Zhang, Z.; Zhang, R. High-corrosion resistance of the microarc oxidation coatings on magnesium alloy obtained in potassium fluotitanate electrolytes. *Surf. Coat. Technol.* **2015**, *264*, 105–113. [CrossRef]

30. Rehman, Z.U.; Ahn, B.H.; Song, J.I.; Koo, B.H. Effect of Na_2SiF_6 concentration on the plasma electrolytic oxidation of AZ31B magnesium alloy. *Int. J. Surf. Sci. Eng.* **2016**, *10*, 456–467. [CrossRef]
31. Kaseem, M.; Yang, H.W.; Ko, Y.G. Toward a nearly defect-free coating via high-energy plasma sparks. *Sci. Rep.* **2017**, *7*, 2378. [CrossRef] [PubMed]
32. Duan, H.; Yan, C.; Wang, F. Effect of electrolyte additives on performance of plasma electrolytic oxidation films formed on magnesium alloy AZ91D. *Electrochim. Acta* **2007**, *52*, 3785–3793. [CrossRef]
33. Shen, M.J.; Wang, X.J.; Zhang, M.F. High-compactness coating grown by plasma electrolytic oxidation on AZ31 magnesium alloy in the solution of silicate–borax. *Appl. Surf. Sci.* **2012**, *259*, 362–366. [CrossRef]
34. Sreekanth, D.; Rameshbabu, N.; Venkateswarlu, K.; Subrahmanyam, C.; Rama Krishna, L.; Prasad Rao, K. Effect of K_2TiF_6 and $Na_2B_4O_7$ as electrolyte additives on pore morphology and corrosion properties of plasma electrolytic oxidation coatings on ZM21 magnesium alloy. *Surf. Coat. Technol.* **2013**, *222*, 31–37. [CrossRef]
35. Sowa, M.; Olesiński, A.; Szumski, B.; Maciej, A.; Bik, M.; Jeleń, P.; Sitarz, M.; Simka, W. Electrochemical characterization of anti-corrosion coatings formed on 6061 aluminum alloy by plasma electrolytic oxidation in the corrosion inhibitor-enriched aqueous solutions. *Electrochim. Acta* **2022**, *424*, 140652. [CrossRef]
36. Senocak, T.C.; Yilmaz, T.A.; Budak, H.F.; Gulten, G.; Yilmaz, A.M.; Ezirmik, K.V.; Totik, Y. Influence of sodium pentaborate ($B_5H_{10}NaO_{13}$) additive in plasma electrolytic oxidation process on WE43 magnesium alloys. *Mater. Today Commun.* **2022**, *30*, 103157. [CrossRef]
37. Florczak, Ł.; Sobkowiak, A.; Nawrat, G. Wpływ heksafluoroantymonianu sodu na właściwości powłok konwersyjnych wytworzonych podczas elektrolitycznego utleniania plazmowego stopu magnezu / The effect of sodium hexafluoroantimonate on the properties of the conversion coatings formed by plasma electrolytic oxidation of a magnesium alloy. *Przemysł Chem.* **2016**, *95*, 1414–1419. [CrossRef]
38. Kokubo, T.; Kushitani, H.; Sakka, S.; Kitsugi, T.; Yamamuro, Y. Solutions able to reproduce in vivo surface-structure changes in bioactive glass-ceramic A-W. *J. Biomed. Mater. Res.* **1990**, *24*, 721–734. [CrossRef]
39. Stern, M.; Geaby, A.L. Electrochemical polarization. *J. Electrochem. Soc.* **1957**, *104*, 56. [CrossRef]
40. Gu, Y.; Bandopadhyay, S.; Chen, C.-f.; Guo, Y.; Ning, C. Effect of oxidation time on the corrosion behavior of micro-arc oxidation produced AZ31 magnesium alloys in simulated body fluid. *J. Alloys Compd.* **2012**, *543*, 109–117. [CrossRef]
41. Xiong, Y.; Hu, Q.; Song, R.; Hu, X. LSP/MAO composite bio-coating on AZ80 magnesium alloy for biomedical application. *Mater. Sci. Eng. C* **2017**, *75*, 1299–1304. [CrossRef]
42. Bordbar-Khiabani, A.; Yarmand, B.; Mozafari, M. Enhanced corrosion resistance and in-vitro biodegradation of plasma electrolytic oxidation coatings prepared on AZ91 Mg alloy using ZnO nanoparticles-incorporated electrolyte. *Surf. Coat. Technol.* **2019**, *360*, 153–171. [CrossRef]
43. Macdonald, D.D.; Sikora, E.; Engelhardt, G. Characterizing electrochemical systems in the frequency domain. *Electrochim. Acta* **1998**, *43*, 87–107. [CrossRef]
44. Available online: https://srdata.nist.gov/xps. (accessed on 1 February 2022).
45. Duan, H.; Yan, C.; Wang, F. Growth process of plasma electrolytic oxidation films formed on magnesium alloy AZ91D in silicate solution. *Electrochim. Acta* **2007**, *52*, 5002–5009. [CrossRef]
46. Zhang, S.-F.; Hu, G.-H.; Zhang, R.-F.; Jia, Z.-X.; Wang, L.-J.; Wang, Y.-J.; Hu, C.-Y.; He, X.-M. Effects of electric parameters on corrosion resistance of anodic coatings formed on magnesium alloys. *Trans. Nonferrous Met. Soc. China* **2010**, *20*, s660–s664. [CrossRef]
47. Sreekanth, D.; Rameshbabu, N.; Venkateswarlu, K. Effect of various additives on morphology and corrosion behavior of ceramic coatings developed on AZ31 magnesium alloy by plasma electrolytic oxidation. *Ceram. Int.* **2012**, *38*, 4607–4615. [CrossRef]
48. Durdu, S.; Bayramoğlu, S.; Demirtaş, A.; Usta, M.; Üçışık, A.H. Characterization of AZ31 Mg Alloy coated by plasma electrolytic oxidation. *Vacuum* **2013**, *88*, 130–133. [CrossRef]
49. Aktuğ, S.L.; Durdu, S.; Kutbay, I.; Usta, M. Effect of $Na_2SiO_3{\cdot}5H_2O$ concentration on microstructure and mechanical properties of plasma electrolytic oxide coatings on AZ31 Mg alloy produced by twin roll casting. *Ceram. Int.* **2016**, *42*, 1246–1253. [CrossRef]
50. Liu, J.; Lu, Y.; Jing, X.; Yuan, Y.; Zhang, M. Characterization of plasma electrolytic oxidation coatings formed on Mg-Li Alloy in an alkaline silicate electrolyte containing silica sol. *Mater. Corros.* **2009**, *60*, 865–870. [CrossRef]
51. Chang, L.-R.; Cao, F.-H.; Cai, J.-S.; Liu, W.-J.; Zhang, Z.; Zhang, J.-Q. Influence of electric parameters on MAO of AZ91D magnesium alloy using alternative square-wave power source. *Trans. Nonferrous Met. Soc. China* **2011**, *21*, 307–316. [CrossRef]
52. Yang, Y.; Wu, H. Effect of current density on corrosion resistance of micro-arc oxide coatings on magnesium alloy. *Trans. Nonferrous Met. Soc. China* **2010**, *20*, s688–s692. [CrossRef]
53. Yang, J.; Lu, X.; Blawert, C.; Di, S.; Zheludkevich, M.L. Microstructure and corrosion behavior of Ca/P coatings prepared on magnesium by plasma electrolytic oxidation. *Surf. Coat. Technol.* **2017**, *319*, 359–369. [CrossRef]
54. Neves, C.S.; Sousa, I.; Freitas, M.A.; Moreira, L.; Costa, C.; Teixeira, J.P.; Fraga, S.; Pinto, E.; Almeida, A.; Scharnagl, N.; et al. Insights into corrosion behaviour of uncoated Mg alloys for biomedical applications in different aqueous media. *J. Mater. Res. Technol.* **2021**, *13*, 1908–1922. [CrossRef]